Computers and Structures 153 (2015) 148–164

Contents lists available at ScienceDirect

Computers and Structures

journal homepage: www.elsevier.com/locate/compstruc

The modal behavior of the MITC3+ triangular shell element

Youngyu Lee [a], Hyeong-Min Jeon [a], Phill-Seung Lee [a,*], Klaus-Jürgen Bathe [b]

[a] Department of Mechanical Engineering, Korea Advanced Institute of Science and Technology, 291 Daehak-ro, Yuseong-gu, Daejeon 305-701, Republic of Korea
[b] Department of Mechanical Engineering, Massachusetts Institute of Technology, Cambridge, MA 02139, USA

ARTICLE INFO

Article history:
Received 9 December 2014
Accepted 24 February 2015
Available online 29 March 2015

Keywords:
Shell structures
Shell finite elements
3-node element
MITC method
Mode analysis

ABSTRACT

In this paper, we investigate the static and dynamic modal behavior of the MITC3+ triangular shell element (Lee and Bathe, 2004; Lee et al., 2014). We focus on bending-dominated situations because such shell problems are particularly difficult to solve when using low-order elements. For comparison, the pure displacement-based (DISP3), MITC3 and MITC4 shell elements are also studied. First, static mode solutions are performed for a single right-angled shell element and an assemblage of two right-angled shell elements. The detailed strain fields are established in the bending modes. This study provides insight into how shear locking occurs on the mode level. We then analytically show how the MITC3+ shell element properly represents the pure bending conditions in a two-sided clamped plate problem. Considering free plate and free hyperboloid shell problems, we finally present the excellent performance of the MITC3+ shell element in dynamic mode solutions.

1. Introduction

Shell structures are ubiquitous in various engineering and scientific fields. In the past decades, the finite element method has been dominantly used to analyze shell structures. In these analyses, it is crucial to use reliable and effective shell finite elements. However, due to the complex and highly sensitive behaviors of shells, it is challenging to develop shell finite elements and, indeed, a great challenge to reach "ideal" (that is, optimal) elements [1–6]. In particular, it is important to obtain an ideal 3-node shell element. Due to its simple geometry defined by only three corner nodes, such an element can be very effectively used in the automatic mesh generation of complex shells.

An ideal shell finite element should uniformly converge with optimal rate in all problems for all asymptotic behaviors (membrane dominated, bending dominated and mixed behaviors) irrespective of the shell geometry, boundary conditions and applied loadings [3–10]. Of course, the shell element should satisfy the ellipticity and consistency conditions. A main difficulty in shell finite element analysis is that the solution accuracy may become drastically worse as the shell thickness decreases. This phenomenon is called locking, which occurs when the element discretization of a shell structure cannot properly represent pure bending displacement fields [4].

To significantly reduce the locking, the MITC method was developed and first applied to develop a 4-node shell element, the MITC4 element [11,12]. Then the method was used to develop higher-order quadrilateral elements [13,14] and a 3-node triangular shell element, the MITC3 element, as well as higher-order triangular shell elements [1,15]. However, the performance of the MITC3 shell element is not as good as of the MITC4 shell element, even though the MITC3 shell element yields much more accurate solutions than the displacement-based 3-node shell element, the DISP3 element [16].

Recently, based on the concept of the MITC3 shell element, a new 3-node triangular MITC3+ shell finite element was developed [2]. The MITC3+ shell element uses a cubic bubble function for the interpolation of the rotations to enrich the bending displacement fields. The corresponding rotation degrees of freedom can be statically condensed out on the element level. A new assumed transverse shear strain field was developed with a new tying scheme to alleviate shear locking while satisfying the consistency and ellipticity conditions. The MITC3+ shell element passes the three basic tests (the patch, zero energy mode and isotropy tests) and shows excellent convergence behaviors in various shell problems even when highly distorted meshes are used [2]. An excellent performance of the MITC3+ shell element in geometric nonlinear analysis was also measured [17]. With such encouraging results at hand, it is clearly of interest to further study this element and identify more deeply its fundamental features.

Our objective in this paper is to present a deeper understanding of the MITC3+ shell element through detailed static and dynamic

* Corresponding author.
E-mail address: phillseung@kaist.edu (P.S. Lee).

http://dx.doi.org/10.1016/j.compstruc.2015.02.033
0045-7949/

mode solutions. The DISP3, MITC3 and MITC4 shell elements are also considered for comparisons. In the static mode solutions of a single right-angled triangular element and an assemblage of two right-angled triangular elements, we investigate the transverse shear strain fields in the bending modes. This study shows how the MITC3+ shell element performs on the mode level. The transverse shear strain fields of the MITC3+ shell element are also studied analytically in a two-sided clamped plate problem, to see whether and how locking occurs. In the dynamic mode solutions, the frequencies and mode shapes are evaluated considering a free square plate problem and a hyperboloid shell problem and the convergence of the frequencies is presented.

In the following sections, we first review the formulations of the 3-node triangular shell finite elements that we consider in this paper and then we present the results of our investigations.

2. Formulations of 3-node triangular shell elements

In this section, the formulations of three 3-node continuum mechanics based triangular shell finite elements are briefly reviewed: the DISP3, MITC3 and MITC3+ shell elements.

2.1. The DISP3 shell element

The geometry of a standard 3-node continuum mechanics based triangular shell finite element is interpolated by [1,3]

$$\vec{x}(r,s,t) = \sum_{i=1}^{3} h_i(r,s)\vec{x}_i + \frac{t}{2}\sum_{i=1}^{3} a_i h_i(r,s)\overrightarrow{V}_n^i \quad \text{with } h_1 = 1-r-s,\ h_2 = r,\ h_3 = s, \tag{1}$$

where $h_i(r,s)$ is the two-dimensional interpolation function of the standard isoparametric procedure corresponding to node i, $\vec{x}_i$ is the position vector of node i in the global Cartesian coordinate system, and a_i and $\overrightarrow{V}_n^i$ denote the shell thickness and the director vector at the node, see Fig. 1.

The corresponding displacement interpolation of the element is given by

$$\vec{u}(r,s,t) = \sum_{i=1}^{3} h_i(r,s)\vec{u}_i + \frac{t}{2}\sum_{i=1}^{3} a_i h_i(r,s)\left(-\overrightarrow{V}_2^i\alpha_i + \overrightarrow{V}_1^i\beta_i\right), \tag{2}$$

in which $\vec{u}_i$ is the nodal displacement vector in the global Cartesian coordinate system, $\overrightarrow{V}_1^i$ and $\overrightarrow{V}_2^i$ are unit vectors orthogonal to $\overrightarrow{V}_n^i$ and to each other, and α_i and β_i are the rotations of the director vector $\overrightarrow{V}_n^i$ about $\overrightarrow{V}_1^i$ and $\overrightarrow{V}_2^i$, respectively, at node i.

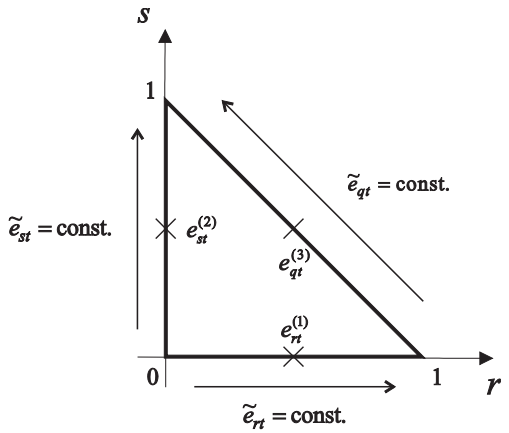

Fig. 2. Tying positions for the assumed transverse shear strain field of the MITC3 shell element. The constant transverse shear strain conditions are imposed along its edges $\left(e_{qt}^{(3)} = \left(e_{st}^{(3)} - e_{rt}^{(3)}\right)/\sqrt{2}\right)$.

The linear part of the displacement-based covariant strain components is given by

$$e_{ij} = \frac{1}{2}(\vec{g}_i \cdot \vec{u}_{,j} + \vec{g}_j \cdot \vec{u}_{,i}), \tag{3}$$

in which

$$\vec{g}_i = \frac{\partial \vec{x}}{\partial r_i}, \quad \vec{u}_{,i} = \frac{\partial \vec{u}}{\partial r_i} \quad \text{with } r_1 = r,\ r_2 = s,\ r_3 = t. \tag{4}$$

The displacement-based 3-node shell finite element has no spurious zero energy mode and satisfies the isotropy condition. However, in bending-dominated problems, this shell finite element is extremely stiff due to shear locking [16].

2.2. The MITC3 shell element

The geometry and displacement interpolations are identical to the DISP3 shell element, but the MITC method is applied [1]. Since the geometry of the 3-node triangular shell finite element is flat, the MITC method is only applied to construct the covariant transverse shear strain field with constant covariant transverse shear strain conditions along the edges. The assumed transverse shear strain field of the MITC3 shell element is given by [1]

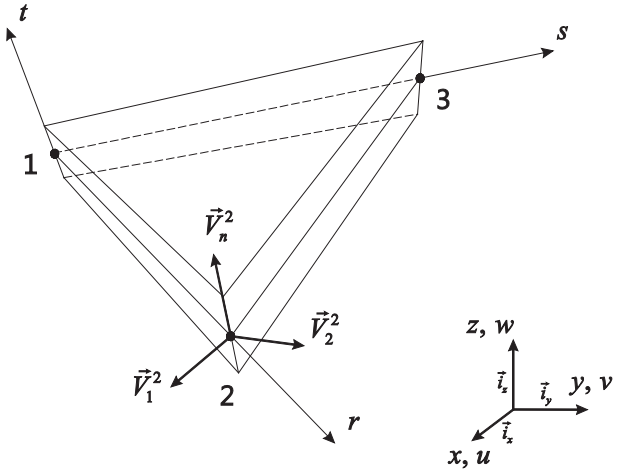

Fig. 1. A standard 3-node triangular continuum mechanics based shell element.

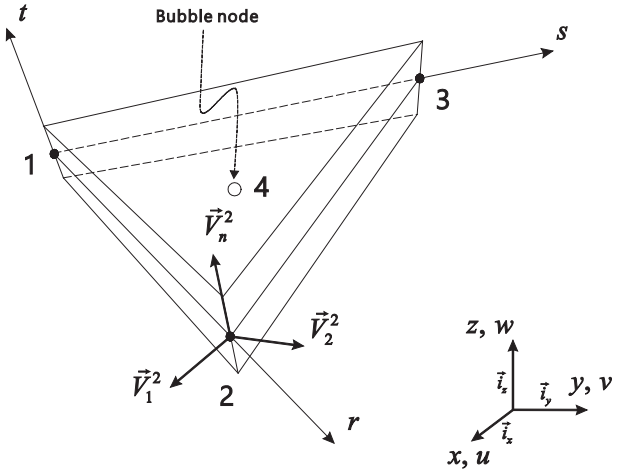

Fig. 3. Geometry of the MITC3+ shell element with an additional bubble node.

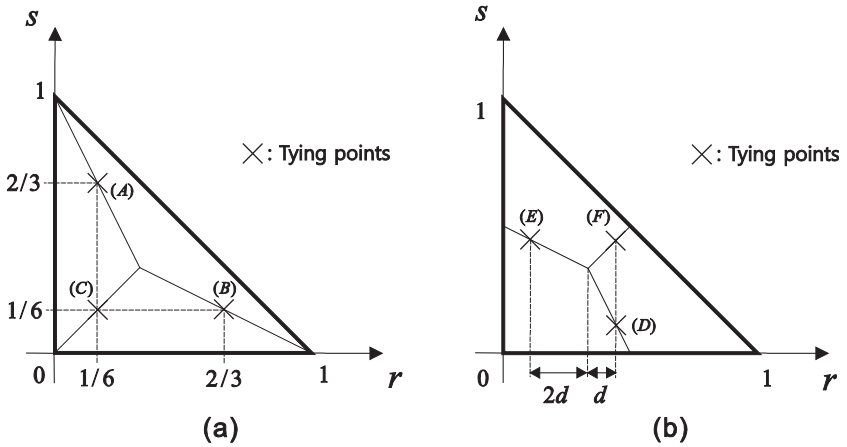

Fig. 4. Tying positions (A)–(F) for the assumed transverse shear strain field of the MITC3+ shell finite element.

Table 1
Tying positions for the assumed transverse shear strain field for the MITC3+ shell element. The distance d is defined in Fig. 4(b).

	Tying positions	r	s
Fig. 4(a)	(A)	1/6	2/3
	(B)	2/3	1/6
	(C)	1/6	1/6
Fig. 4(b)	(D)	$1/3+d$	$1/3-2d$
	(E)	$1/3-2d$	$1/3+d$
	(F)	$1/3+d$	$1/3+d$

$$\tilde{e}_{rt}^{MITC3} = e_{rt}^{(1)} + cs, \quad \tilde{e}_{st}^{MITC3} = e_{st}^{(2)} - cr, \tag{5}$$

in which $c = e_{rt}^{(3)} - e_{rt}^{(1)} - e_{st}^{(3)} + e_{st}^{(2)}$ and the tying points are shown in Fig. 2.

The MITC3 shell element passes the basic tests: zero energy mode, isotropy and patch tests. The MITC3 shell element shows a quite reasonable convergence behavior. However, as the thickness decreases, some locking occurs in bending-dominated problems [1].

2.3. The MITC3+ shell element

The geometry of the MITC3+ shell element, see Fig. 3, is interpolated by

$$\vec{x}(r,s,t) = \sum_{i=1}^{3} h_i(r,s)\vec{x}_i + \frac{t}{2}\sum_{i=1}^{4} a_i f_i(r,s)\vec{V}_n^i$$
$$\text{with } a_4\vec{V}_n^4 = \frac{1}{3}\left(a_1\vec{V}_n^1 + a_2\vec{V}_n^2 + a_3\vec{V}_n^3\right), \tag{6}$$

in which $f_i(r,s)$ are the two-dimensional interpolation functions with the cubic bubble function f_4 corresponding to the internal node 4

$$f_1 = h_1 - \frac{1}{3}f_4, \quad f_2 = h_2 - \frac{1}{3}f_4, \quad f_3 = h_3 - \frac{1}{3}f_4, \quad f_4 = 27rs(1-r-s). \tag{7}$$

From Eq. (6), the displacement interpolation is described by

$$\vec{u}(r,s,t) = \sum_{i=1}^{3} h_i(r,s)\vec{u}_i + \frac{t}{2}\sum_{i=1}^{4} a_i f_i(r,s)\left(-\vec{V}_2^i\alpha_i + \vec{V}_1^i\beta_i\right), \tag{8}$$

where α_4 and β_4 are the rotation degrees of freedom at the internal node [2]. These additional rotation degrees of freedom can be condensed out on the element level.

Unlike the standard 3-node shell elements, the MITC3+ shell element has an internal node and the corresponding cubic bubble function in the geometry and displacement interpolations. The internal node with only rotation degrees of freedom is positioned on the flat surface defined by the three corner nodes of the element. Hence, the geometry of the MITC3+ shell element is

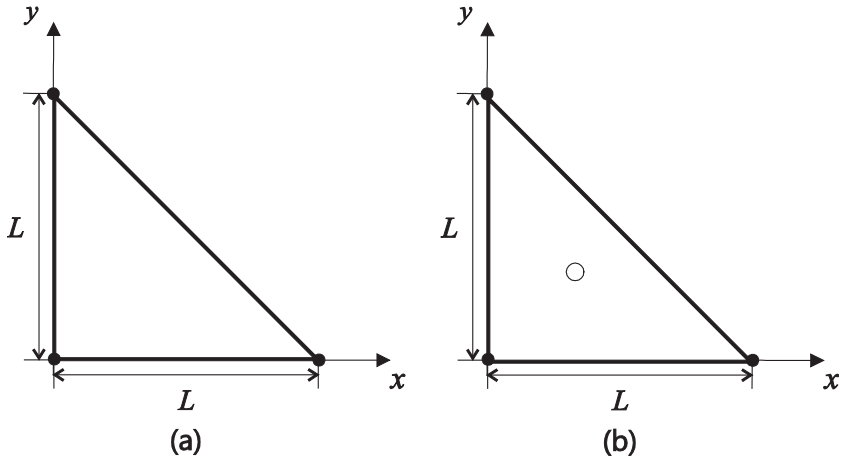

Fig. 5. A single right-angled triangular shell element in plate bending ($L = 1.0, a/L = 1/10,000, E = 1.7472 \times 10^7$ and $\nu = 0.3$). (a) A single 3-node triangular shell element. (b) A single 3-node triangular shell element with a bubble node on rotations.

Table 2
Eigenvalues of the stiffness matrix of the single triangular shell element for the element geometry shown in Fig. 5. Note that modes 1 to 6 produce zero eigenvalues corresponding to rigid body modes. The order of the zero eigenvalues calculated is smaller than 10^{-12}.

Mode	DISP3		MITC3		MITC3+	
7	2.8000E+01	T	6.6764E−07	B1	6.6685E−07	B1
8	2.8000E+01	B1	8.1455E−07	B2	7.9621E−07	B2
9	2.8000E+01	B2	2.4924E−06	B3	2.4921E−06	B3
10	2.8000E+01	B3	3.6928E+01	T	8.3107E−06	B1+
11	4.4800E+02	S1	4.6707E+02	S1	1.3599E−05	T
12	8.3813E+02	M	8.3813E+02	M	1.4128E−05	B2+
13	1.1200E+03	S2	1.1760E+03	S2	4.6667E+02	S1
14	1.3440E+03	M	1.3440E+03	M	8.3813E+02	M
15	3.0019E+03	M	3.0019E+03	M	1.1760E+03	S2
16	–		–		1.3440E+03	M
17	–		–		3.0019E+03	M

B: symmetric bending modes, T: in-plane twisting mode, S: transverse shearing modes, M: membrane modes, B+: anti-symmetric bending modes due to the bubble function enrichment.

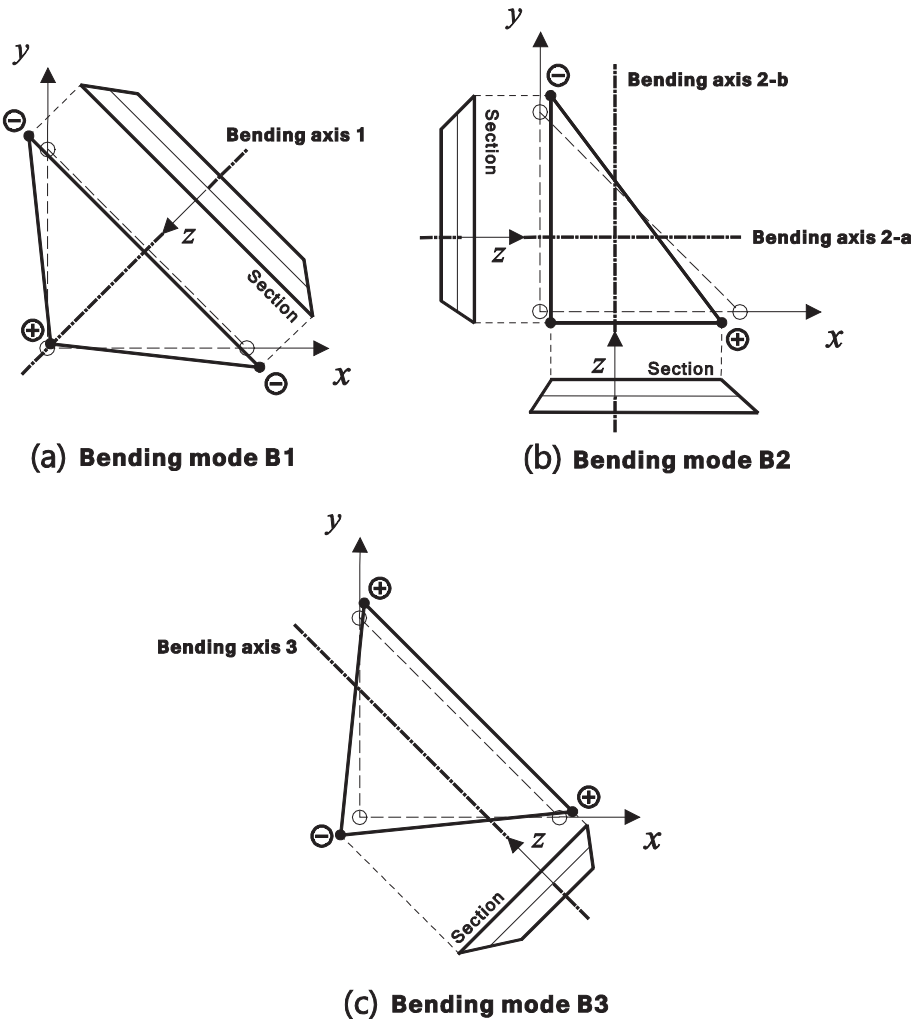

Fig. 6. Shapes of the bending modes for the single right-angled MITC3 shell element shown in Fig. 5(a). The dotted and solid lines correspond to the top surfaces before and after deformation, respectively, on the *xy*-plane. Plus and minus signs denote small out-of-plane displacements in the *z* and –*z* directions, respectively.

always flat and only the transverse shear strain components are established using the MITC method.

The assumed transverse shear strain field of the MITC3+ shell finite element is given by [2]

$$\hat{e}_{rt}^{MITC3+} = \frac{2}{3}\left(e_{rt}^{(B)} - \frac{1}{2}e_{st}^{(B)}\right) + \frac{1}{3}\left(e_{rt}^{(C)} + e_{st}^{(C)}\right) + \frac{1}{3}\hat{c}(3s-1),$$
$$\hat{e}_{st}^{MITC3+} = \frac{2}{3}\left(e_{st}^{(A)} - \frac{1}{2}e_{rt}^{(A)}\right) + \frac{1}{3}\left(e_{rt}^{(C)} + e_{st}^{(C)}\right) + \frac{1}{3}\hat{c}(1-3r), \quad (9)$$

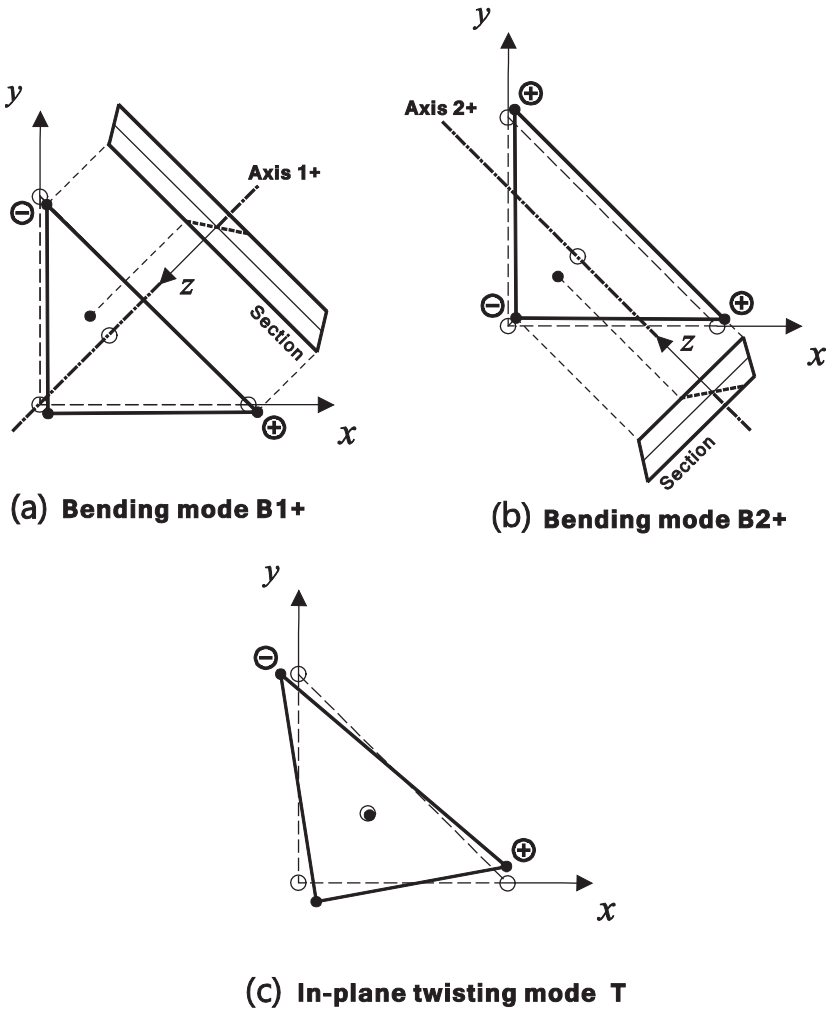

Fig. 7. Mode shapes of the single right-angled MITC3+ shell element shown in Fig. 5(b). The dotted and solid lines correspond to the top surfaces before and after deformation, respectively, on the *xy*-plane. Plus and minus signs denote small out-of-plane displacements in the *z* and –*z* directions, respectively.

Table 3
Strain fields of the single right-angled DISP3 and MITC3 shell elements in the bending modes B1, B2 and B3. $a/L = 1/10,000,\ z = a(t/2)$.

Bending mode		DISP3	MITC3
B1	Eigenvalue	2.8000E+01	6.6764E−07
	Bending	$\varepsilon_{xx} = 0.280z$	$\varepsilon_{xx} = 0.269z$
	Strains	$\varepsilon_{yy} = 0.280z$	$\varepsilon_{yy} = 0.269z$
		$\gamma_{xy} = -1.38z$	$\gamma_{xy} = -1.36z$
	Transverse	$\gamma_{xz} = 0.137 + 0.280r - 0.691s$	$\gamma_{xz} = 0.0$
	shear strains	$\gamma_{yz} = 0.137 - 0.691r + 0.280s$	$\gamma_{yz} = 0.0$
B2	Eigenvalue	2.8000E+01	8.1455E−07
	Bending	$\varepsilon_{xx} = -z$	$\varepsilon_{xx} = -0.853z$
	Strains	$\varepsilon_{yy} = z$	$\varepsilon_{yy} = 0.853z$
		$\gamma_{xy} = 0.0$	$\gamma_{xy} = 0.0$
	Transverse	$\gamma_{xz} = 0.5 - r - 0.5s$	$\gamma_{xz} = 0.0$
	shear strains	$\gamma_{yz} = -0.5 + 0.5r + s$	$\gamma_{yz} = 0.0$
B3	Eigenvalue	2.8000E+01	2.4924E−06
	Bending	$\varepsilon_{xx} = 0.960z$	$\varepsilon_{xx} = 0.963z$
	strains	$\varepsilon_{yy} = 0.960z$	$\varepsilon_{yy} = 0.963z$
		$\gamma_{xy} = 1.45z$	$\gamma_{xy} = 1.42z$
	Transverse	$\gamma_{xz} = -0.561 + 0.960r + 0.723s$	$\gamma_{xz} = 0.0$
	shear strains	$\gamma_{yz} = -0.561 + 0.723r + 0.960s$	$\gamma_{yz} = 0.0$

in which $\hat{c} = e_{rt}^{(F)} - e_{rt}^{(D)} - e_{st}^{(F)} + e_{st}^{(E)}$ and the 6 tying points (A)–(F) with the tying distance d are defined in Fig. 4 and Table 1. A fixed value $d = 1/10,000$ is suggested in Ref. [2].

The MITC3+ shell element passes the basic tests: zero energy mode, isotropy and patch tests. An excellent convergence behavior is seen considering various thicknesses and element distortions [2].

Table 4
Strain fields of the single right-angled MITC3+ shell element in the bending modes B1+ and B2+, and in-plane twisting mode T. $a/L = 1/10,000,\ z = a(t/2)$.

Bending mode B1+	Eigenvalue	8.3107E−06
	Bending strains	$\varepsilon_{xx} = [0.019 - 21.3(s - 2rs - s^2)]z$
		$\varepsilon_{yy} = [-0.019 + 21.3(r - 2rs - r^2)]z$
		$\gamma_{xy} = -21.3(r - s - r^2 + s^2)z$
	Transverse shear strains	$\gamma_{xz} = 0.0$
		$\gamma_{yz} = 0.0$
Bending mode B2+	Eigenvalue	1.4128E−05
	Bending strains	$\varepsilon_{xx} = [-0.001 - 21.8(s - 2rs - s^2)]z$
		$\varepsilon_{yy} = [-0.001 - 21.8(r - 2rs - r^2)]z$
		$\gamma_{xy} = [-0.064 - 21.8(r + s - 4rs - r^2 - s^2)]z$
	Transverse shear strains	$\gamma_{xz} = 0.0$
		$\gamma_{yz} = 0.0$
In-plane twisting mode T ($d = 1/10,000$)	Eigenvalue	1.3599E−05
	Bending strains	$\varepsilon_{xx} = [-0.514 + 1.49(s - 2rs - s^2)]z$
		$\varepsilon_{yy} = [0.514 - 1.49(r - 2rs - r^2)]z$
		$\gamma_{xy} = 1.49(r - s - r^2 + s^2)z$
	Transverse shear strains	$\gamma_{xz} = 1.99d(1 - 3s)$
		$\gamma_{yz} = 1.99d(-1 + 3r)$

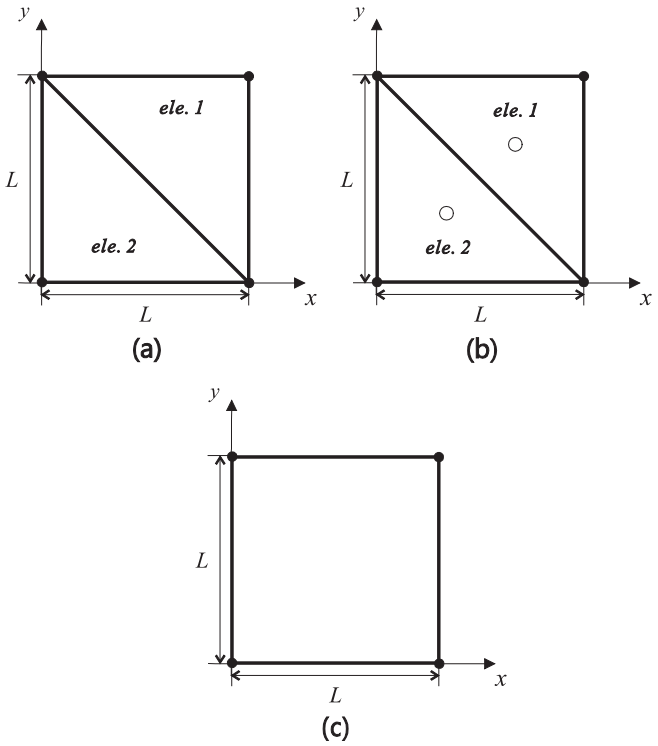

Fig. 8. An assemblage of two right-angled triangular elements ($L = 1.0$, $E = 1.7472 \times 10^7$ and $v = 0.3$). (a) Assemblage of two 3-node triangular shell elements. (b) Assemblage of two 3-node triangular shell elements with bubble nodes on rotations. (c) A single 4-node quadrilateral shell element.

3. Static mode solutions

In this section, we perform the static mode solutions of the DISP3, MITC3 and MITC3+ shell elements considering two plate bending cases: a single right-angled triangular shell element and an assemblage of two right-angled triangular shell elements. Note that membrane locking is not present because the geometry of the 3-node triangular shell elements is flat.

Table 5
Eigenvalues of the stiffness matrix of the assemblage of two right-angled triangular shell elements shown in Fig. 8 when $a/L = 1/10,000$. Note that modes 1 to 6 produce zero eigenvalues corresponding to rigid body modes. The order of the zero eigenvalues calculated is smaller than 10^{-12}.

Mode	MITC4		MITC3		MITC3+	
7	7.2000E−07	BL1	9.9556E−07	BC1	9.3805E−07	BC1
8	7.2000E−07	BL2	1.1200E−06	BC2	1.0608E−06	BC2
9	9.9556E−07	BC1	2.0800E−06	BC3	1.9629E−06	BC3
10	1.1200E−06	BC2	3.2000E−06	BL2	3.0544E−06	BL2
11	2.0800E−06	BC3	3.4167E+01	BL1	8.9316E−06	BQ1+
12	5.6000E+01	TQ	5.6000E+01	TQ	1.1912E−05	BQ2+
13	5.0400E+02	BC4	8.4000E+02	SQ1	1.4173E−05	TQ
14	8.4000E+02	SQ1	9.1783E+02	SQ2	1.5159E−05	BL1
15	8.4000E+02	SQ2	1.3440E+03	MQ	1.6660E−05	BQ3+
16	8.6400E+02	MQ	1.3440E+03	MQ	9.3333E+01	BQ4+
17	8.6400E+02	MQ	1.3440E+03	MQ	8.0267E+02	SQ1
18	1.3440E+03	MQ	1.5120E+03	BC4	8.4000E+02	SQ2
19	1.3440E+03	MQ	2.4960E+03	MQ	1.3440E+03	MQ
20	2.4960E+03	MQ	3.8400E+03	MQ	1.3440E+03	MQ
21	-		-		1.3440E+03	MQ
22	-		-		1.5493E+03	BC4
23	-		-		2.4960E+03	MQ
24	-		-		3.8400E+03	MQ

BC: bending modes with constant bending strain fields, BL: bending modes with linear bending strain fields, TQ: in-plane twisting mode, SQ: transverse shearing modes, MQ: membrane modes, BQ+: bending modes due to the bubble function enrichment.

For the static mode solution, the following eigenvalue problem is considered

$$\mathbf{K}\vec{\phi}_i^s = \lambda_i^s \vec{\phi}_i^s \quad \text{with } i = 1, 2, \ldots, N, \tag{10}$$

where $\mathbf{K}$ is the stiffness matrix, λ_i^s and $\vec{\phi}_i^s$ are the eigenvalue and orthonormal eigenvector of the ith static mode, respectively, and N is the number of degrees of freedom [3]. The eigenvector represents a deformation mode and the corresponding eigenvalue is twice the strain energy stored in these displacements, since $\vec{\phi}_i^{sT}\vec{\phi}_i^s = 1$.

For the deformation mode $\vec{\phi}_i^s$, the strain fields defined in the global Cartesian coordinate are

$$\vec{\varepsilon} = \boldsymbol{B}\vec{\phi}_i^s \quad \text{with } \vec{\varepsilon} = \begin{bmatrix} \varepsilon_{xx} & \varepsilon_{yy} & \gamma_{xy} & \gamma_{xz} & \gamma_{yz} \end{bmatrix}^T, \tag{11}$$

where $\boldsymbol{B}$ is the strain–displacement relation matrix obtained in the finite element formulation.

Using the above relations, we can study the detailed strain behavior of shell finite elements in each eigenvector mode. Since shell finite elements should produce zero transverse shear strains in the bending modes, important insight into shear locking of an element can be obtained when considering the eigenvectors.

3.1. Single right-angled triangular element

As shown in Fig. 5, we consider a single right-angled triangular shell element with free boundary (length $L = 1.0$, thickness to length ratio $a/L = 1/10,000$, Young's modulus $E = 1.7472 \times 10^7$ and Poisson's ratio $v = 0.3$). The static mode solutions are performed for the DISP3, MITC3 and MITC3+ shell finite elements, and we focus on the static modes related to plate bending.

The eigenvalues of the stiffness matrices of the DISP3, MITC3 and MITC3+ shell elements are presented in Table 2. The modes are named based on their fundamental kinematics (bending, in-plane twisting, transverse shearing, and membrane kinematics). While the DISP3 and MITC3 shell elements have the 3 symmetric

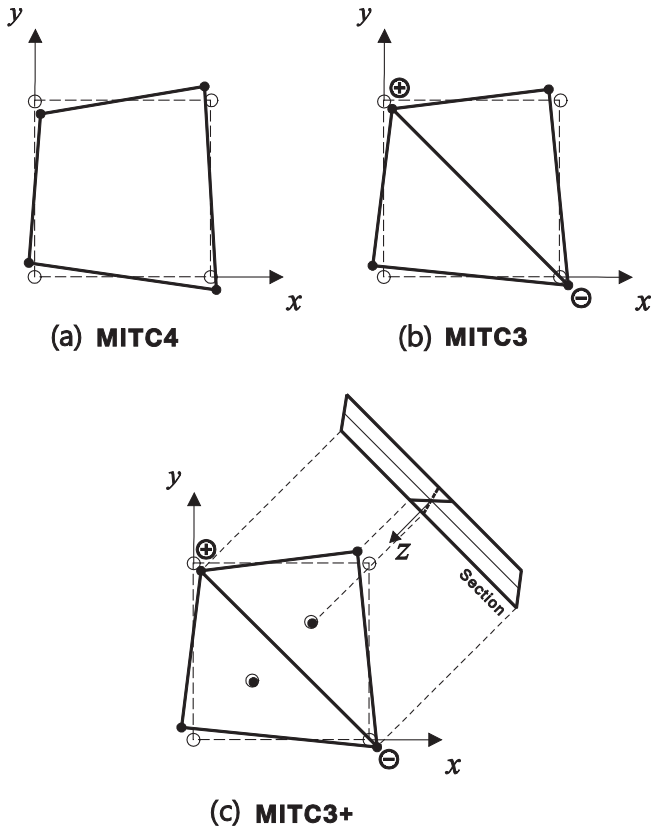

Fig. 9. Shapes of the bending mode BL1 shown in Fig. 8. The dotted and solid lines correspond to the top surfaces before and after deformation, respectively, on the *xy*-plane. Plus and minus signs denote small out-of-plane displacements in the *z* and –*z* directions, respectively.

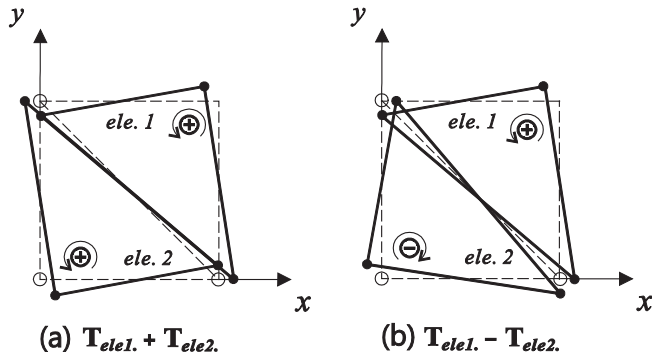

Fig. 10. In-plane twisting of two 3-node triangular shell elements. The dotted and solid lines correspond to the top surfaces before and after deformation, respectively, in the *xy*-plane.

bending modes B1, B2, and B3 shown in Fig. 6, the MITC3+ shell element has 2 additional anti-symmetric bending modes B1+ and B2+ shown in Fig. 7(a) and (b) due to the bubble function enrichment on rotations [18]. Note that the anti-symmetric bending modes B1+ and B2+ "correspond" to the symmetric bending modes B1 and B3, respectively. It is observed that, in the bending modes B1, B2 and B3, the eigenvalues of the DISP3 shell element are much larger than those of the MITC3 and MITC3+ shell elements. That is, the DISP3 shell element is much stiffer. Another important observation is that the MITC3+ shell element contains a much more flexible in-plane twisting mode T than the MITC3 shell element.

We next investigate the transverse shearing behavior of the DISP3, MITC3 and MITC3+ shell elements on the deformation mode level. The bending modes B1, B2, B3, B1+ and B2+ are considered. Note that the transverse shear strains γ_{xz} and γ_{yz} should be zero in the bending modes. Table 3 summarizes the strain fields of the DISP3 and MITC3 shell elements obtained by Eq. (11) in the bending modes. Obviously, the DISP3 shell element produces non-zero transverse shear strains in all bending modes, that is, the element severely locks.

However, the MITC3 shell element produces zero transverse shear strains in the bending modes B1, B2 and B3. Hence the shear locking is completely removed on the *element* level. A further analysis shows that the same observation holds for a single MITC3 triangular element of arbitrary shape. However, it is important to note that, nevertheless, the MITC3 shell element still shows shear locking on the element *assemblage* level, see the convergence test results in Refs. [1,2,16,19]. Of course, the locking is much less severe than for the DISP3 shell element.

The MITC3+ shell element also gives zero transverse shears in the bending modes B1, B2 and B3. In addition, Table 4 presents the strain fields in the bending modes B1+ and B2+ and shows that in these bending modes, as well, zero transverse shear strains are seen.

Table 6
Eigenvalues of the stiffness matrix of the assemblage of two MITC3+ shell elements shown in Fig. 8(b) according to the tying distance *d* in the plate bending problem when $a/L = 1/10,000$. Note that modes 1 to 6 produce zero eigenvalues corresponding to rigid body modes. The order of the zero eigenvalues calculated is smaller than 10^{-12}. Modes 19–21, 23 and 24 are membrane modes. For $d = 1/10,000$, the eigenvalues are given in Table 5.

Mode	*d*							
	1/100		1/1,000		1/100,000		0.0	
7	9.3805E−07	BC1	9.3805E−07	BC1	9.3805E−07	BC1	9.3805E−07	BC1
8	1.0611E−06	BC2	1.0611E−06	BC2	1.0545E−06	BC2	1.0099E−06	BL1
9	1.9629E−06	BC3	1.9629E−06	BC3	1.1303E−06	BL1	1.0522E−06	BC2
10	3.0544E−06	BL2	3.0544E−06	BL2	1.5394E−06	TQ	1.4140E−06	TQ
11	9.7882E−06	BQ1+	9.7846E−06	BQ1+	1.9629E−06	BC3	1.9629E−06	BC3
12	1.1912E−05	BQ2+	1.1912E−05	BQ2+	3.0544E−06	BL2	3.0544E−06	BL2
13	1.6660E−05	BQ3+	1.6660E−05	BQ3+	1.0320E−05	BQ1+	1.0312E−05	BQ1+
14	1.2767E−01	TQ	1.2782E−03	TQ	1.1912E−05	BQ2+	1.1912E−05	BQ2+
15	1.2768E−01	BL1	1.2783E−03	BL1	1.6660E−05	BQ3+	1.6660E−05	BQ3+
16	9.3340E+01	BQ4+	9.3333E+01	BQ4+	9.3333E+01	BQ4+	9.3333E+01	BQ4+
17	8.0267E+02	SQ1	8.0267E+02	SQ1	8.0267E+02	SQ1	8.0267E+02	SQ1
18	8.4001E+02	SQ2	8.4000E+02	SQ2	8.4000E+02	SQ2	8.4000E+02	SQ2
22	1.5493E+03	BC4	1.5493E+03	BC4	1.5493E+03	BC4	1.5493E+03	BC4

BC: bending modes with constant bending strain fields, BL: bending modes with linear bending strain fields, TQ: in-plane twisting mode, SQ: transverse shearing modes, BQ+: bending modes due to the bubble function enrichment.

Table 7
Strain fields of the MITC4, MITC3 and MITC3+ shell elements in the bending mode BL1. $a/L = 1/10,000, \quad z = a(t/2)$.

MITC4 Eig.: 7.2000E−07	MITC3 (*ele. 1*) Eig.: 3.4167E+01	MITC3+ (*ele. 1*, $d = 0$) Eig.: 1.0099E−06
$\varepsilon_{xx} = -0.403sz$ $\varepsilon_{yy} = 0.915rz$ $\gamma_{xy} = (-0.403r + 0.915s)z$	$\varepsilon_{xx} = -0.675z$ $\varepsilon_{yy} = 0.675z$ $\gamma_{xy} = 0.0$	$\varepsilon_{xx} = [-0.670 - 0.401(s - 2rs - s^2)]z$ $\varepsilon_{yy} = [0.670 + 0.401(r - 2rs - r^2)]z$ $\gamma_{xy} = 0.401(-r + s + r^2 - s^2)z$
$\gamma_{xz} = 0.0$ $\gamma_{yz} = 0.0$	$\gamma_{xz} = -0.235 + 0.675s$ $\gamma_{yz} = 0.235 - 0.675r$	$\gamma_{xz} = -1.34d(1 - 3s)$ $\gamma_{yz} = -1.34d(-1 + 3r)$

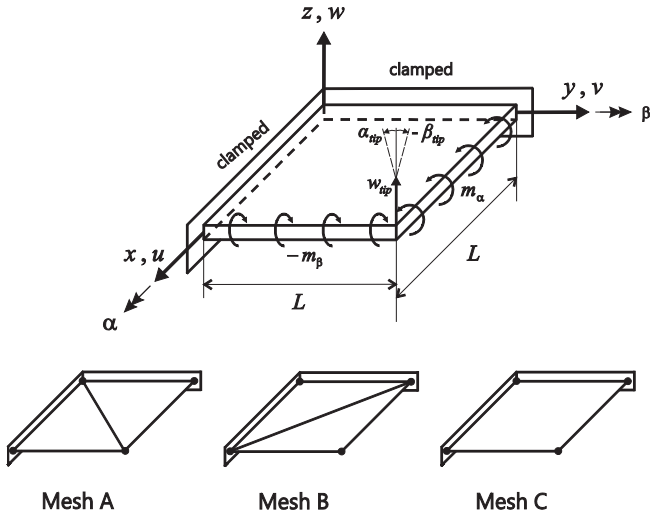

Fig. 11. Two-sided clamped plate problem ($L = 1.0, m_\alpha = m_\beta = 2/L, \quad E = 1.7472 \times 10^7$ and $\nu = 0.0$) and meshes used for the MITC3+ shell elements (Meshes A and B) and the MITC4 shell element (Mesh C).

We also investigate the strain fields of the MITC3+ shell element in the in-plane twisting mode T shown in Fig. 7(c). Table 4 shows that the transverse shear strains in the in-plane twisting mode depend on the tying distance d defined in Fig. 4(b) and Table 1. In Refs. [2,19], we observed that the performance of the 3-node shell element can be improved by reducing the transverse shear strains in the in-plane twisting mode. In the following section, we study how the in-plane twisting mode affects the modal behavior.

3.2. Assemblage of two right-angled triangular elements

We consider an assemblage of two right-angled triangular shell elements with free boundary as shown in Fig. 8(a) and (b). The static mode solution is performed for the MITC3 and MITC3+ shell elements, and, for comparison, a single MITC4 shell element is also tested, see Fig. 8(c). We use $a/L = 1/10,000, E = 1.7472 \times 10^7$ and $\nu = 0.3$.

Table 5 presents the eigenvalues of the stiffness matrices of the MITC4, MITC3 and MITC3+ models. The deformation modes are named based on their kinematics (bending, in-plane twisting, transverse shearing, and membrane kinematics). All shell element models produce 6 bending modes BC1, BC2, BC3, BC4, BL1 and BL2, and the MITC3+ shell element additionally produces 4 bending modes BQ1+, BQ2+, BQ3+ and BQ4+ due to the bubble function enrichment on rotations. It is seen that, in the bending mode BL1 shown in Fig. 9, the MITC3 shell element shows a much stiffer behavior than the MITC4 and MITC3+ shell elements. Compared to the MITC3 shell element, the MITC3+ shell element is much more flexible in the bending mode BL1 and in the in-plane twisting mode TQ.

In Ref. [2], we observed that, for a *single* MITC3+ shell element, as the tying distance d decreases, the eigenvalue corresponding to the in-plane twisting mode T decreases and is zero when $d = 0$. Considering now the assemblage of the MITC3+ shell elements shown in Fig. 8(b), we also perform the eigenvalue test by varying the tying distance d. Table 6 presents the eigenvalues of the assemblage of the two MITC3+ shell elements. As the tying distance d decreases (that is, the eigenvalue of the in-plane twisting mode T of a single MITC3+ element becomes smaller), the eigenvalues corresponding to the bending mode BL1 and in-plane twisting mode TQ decrease together. This fact implies that the in-plane twisting acts together with the bending mode BL1. In Table 6, we also show that, unlike for a single MITC3+ shell element [2], a zero eigenvalue is not present when $d = 0$. The reason is graphically explained in Fig. 10, which shows that the in-plane twisting mode of an assemblage of two triangular shell elements cannot be activated like for a single triangular shell element [2,20].

Table 7 presents the strain fields for the MITC4, MITC3 and MITC3+ shell elements to investigate the shear locking behavior in the bending mode BL1. For the MITC4 shell element, the bending mode BL1 produces linear bending strain fields for $\varepsilon_{xx}, \varepsilon_{yy}$ and γ_{xy} (that is, the strain fields are linear functions of r and s) and zero

Table 9
Strain energies for the two-sided clamped plate problem shown in Fig. 11 using the Mesh A with the MITC3+ shell element according to the tying distance d.

a/L	d			
	d = 1/100	d = 1/1,000	d = 1/10,000	d = 1/100,000
1/100	1.5589E−01	4.7837E−01	4.8848E−01	4.8858E−01
1/1,000	2.2787E+00	1.5587E+02	4.7820E+02	4.8830E+02
1/10,000	2.2893E+01	2.2787E+03	1.5587E+05	4.7820E+05

Table 8
Strain energies for the two-sided clamped plate problem shown in Fig. 11. The tying distance $d = 0$ is used for the MITC3+ shell element.

a/L	MITC3		MITC3+		MITC4
	Mesh A	Mesh B	Mesh A	Mesh B	Mesh C
1/100	4.1190E−04	6.8681E−01	4.8858E−01	6.8681E−01	1.0989E+00
1/1,000	4.1209E−03	6.8681E+02	4.8840E+02	6.8681E+02	1.0989E+03
1/10,000	4.1209E−02	6.8681E+05	4.8840E+05	6.8681E+05	1.0989E+06
Order of change	a/L	$(a/L)^3$	$(a/L)^3$	$(a/L)^3$	$(a/L)^3$

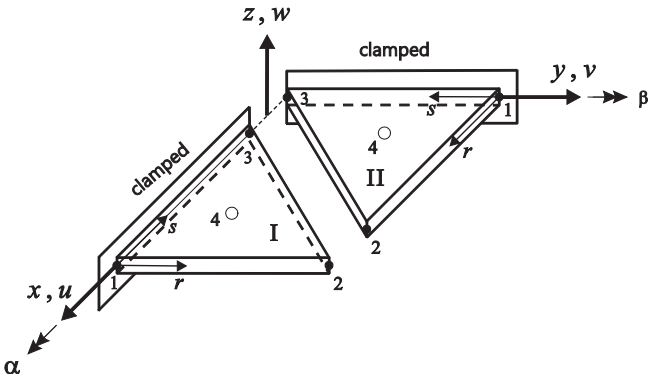

Fig. 12. Element node numbers for the two-sided clamped plate problem using the MITC3+ shell elements with Mesh A shown in Fig. 11.

Table 10
Frequencies of the modes 7–11 for the free square plate problem shown in Fig. 13 with $N \times N$ meshes when $a/L = 1/1,000$.

Shell elements	N	Mode number				
		7	8	9	10	11
MITC4	5	21.366	31.922	40.568	57.223	57.223
	10	21.094	30.915	38.547	55.067	55.067
	15	21.040	30.714	38.153	54.619	54.619
	20	21.021	30.642	38.015	54.459	54.459
MITC3	5	21.738	31.964	40.687	60.007	118.46
	10	21.647	30.986	38.684	57.523	101.67
	15	21.576	30.787	38.284	56.845	98.340
	20	21.468	30.710	38.129	56.273	84.032
MITC3+	5	21.247	31.677	40.017	57.568	57.908
	10	21.051	30.862	38.431	55.088	55.451
	15	21.011	30.690	38.103	54.601	54.783
	20	20.998	30.629	37.986	54.434	54.540
Ref.		21.000	30.564	37.864	54.284	54.284

*The reference solutions are obtained by 50×50 element meshes of the MITC4 shell element.

transverse shear strains. The bending mode BL1 of the MITC3 shell elements produces constant bending strain fields and non-zero transverse shear strains, that is, shear locking occurs in the element assemblage. However, with the help of the bending mode B1+ of a single MITC3+ shell element, in the bending mode BL1, the MITC3+ shell element produces bending strain fields up to quadratic order for $\varepsilon_{xx}, \varepsilon_{yy}$ and γ_{xy} and zero transverse shear strains when $d = 0$. Hence, in the bending mode BL1, shear locking can be alleviated with a small value of d and is completely removed with $d = 0$.

In summary, for the MITC3+ element, an enriched bending strain field is provided through the bending mode BL1 for the two element assemblage. The shear locking in this mode is alleviated by controlling the stiffness in the in-plane twisting mode T of a single MITC3+ shell element. This behavior is not present in the MITC3 shell element, which does not lock on the element level, but locks in the two element assemblage due to a deficiency of pure bending modes.

4. Two-sided clamped plate problem

In this section, we study the behavior of the MITC3+ shell element in the two-sided clamped plate of dimension $L \times L$ shown Fig. 11 ($L = 1.0, E = 1.7472 \times 10^7$ and $\nu = 0$). The plate is subjected to uniform moments m_α and $-m_\beta$ along its free sides. The boundary conditions are $u = v = w = \alpha = \beta = 0$ along the two clamped edges.

This plate problem was used to investigate the shear locking behavior of 3-node triangular shell elements in Ref. [16], which reports that, while the MITC3 shell element does not lock in Mesh B, the shell element severely locks in Mesh A. In general, triangular shell elements show such stiff behavior in Mesh A due to shear locking. To improve the performance of 3-node triangular

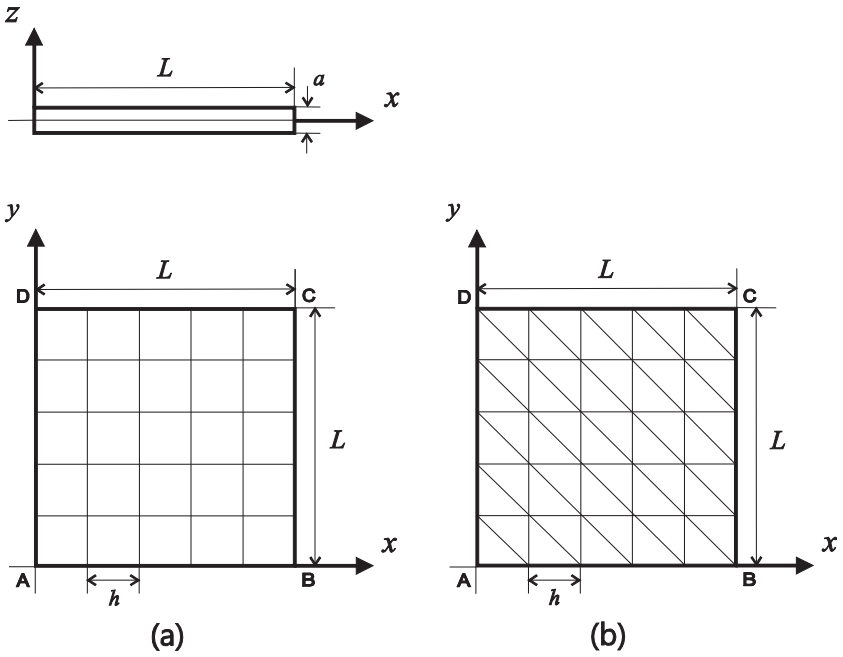

Fig. 13. Free square plate problem for dynamic mode analysis with 2 different 5×5 mesh patterns ($L = 1.0, E = 2.07 \times 10^{11}$, $\nu = 0.3$ and $\rho = 7.8 \times 10^3$). (a) Mesh pattern used for the MITC4 shell element. (b) Mesh pattern used for the MITC3 and MITC3+ shell elements.

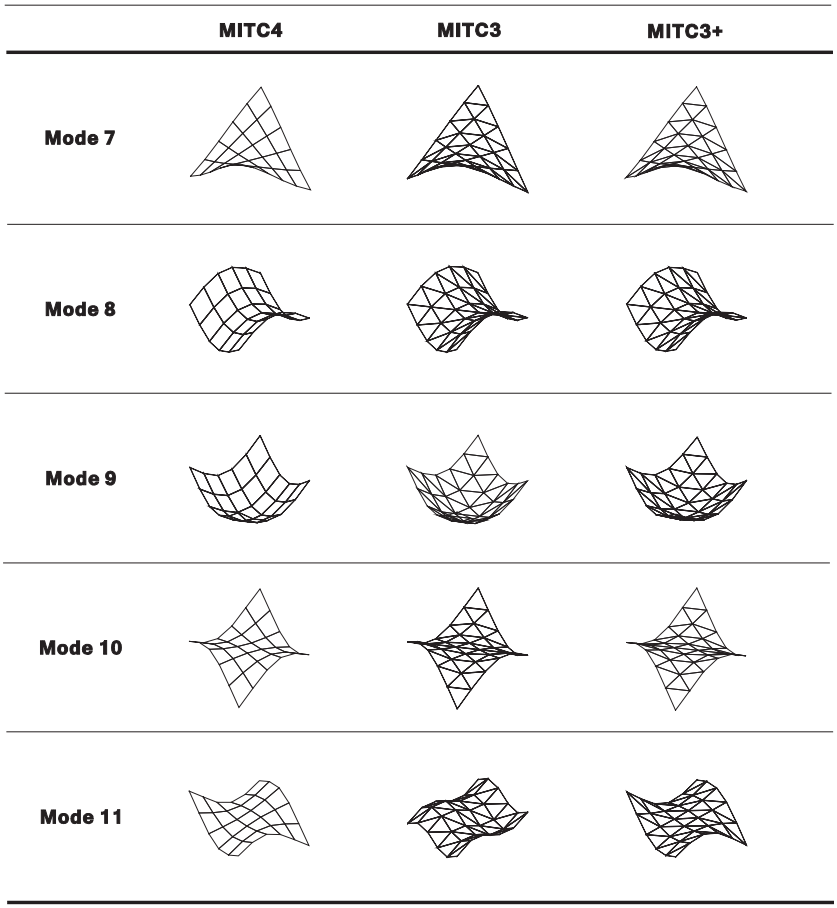

Fig. 14. Shapes of the modes 7–11 for the free square plate problem shown in Fig. 13 with 5×5 element meshes when $a/L = 1/1,000$.

shell elements, this phenomenon should be overcome. Hence, we investigate the effectiveness of the MITC3+ shell element in the analysis of this two-sided clamped plate problem.

4.1. Transverse shear strain fields

Using the two MITC3+ shell elements, the two-sided clamped plate is modeled as shown by element-I and element-II in Fig. 12. The geometry of the elements is given by the following nodal positions

$$\begin{aligned} &x_1 = 1, y_1 = 0,\ \ x_2 = 1, y_2 = 1,\ \ x_3 = 0, y_3 = 0,\ \ x_4 = 2/3, y_4 = 1/3 \ \text{ for element-I},\\ &x_1 = 0, y_1 = 1,\ \ x_2 = 1, y_2 = 1,\ \ x_3 = 0, y_3 = 0,\ \ x_4 = 1/3, y_4 = 2/3 \ \text{ for element-II}, \end{aligned} \tag{12}$$

where the subscripts are the node numbers on the element level, see Fig. 12.

The boundary condition of the elements is given by

$$\begin{aligned} &u_1 = u_3 = v_1 = v_3 = w_1 = w_3 = \alpha_1 = \alpha_3 = \beta_1 = \beta_3 = 0 \ \text{ for element-I},\\ &u_1 = u_3 = v_1 = v_3 = w_1 = w_3 = \alpha_1 = \alpha_3 = \beta_1 = \beta_3 = 0 \ \text{ for element-II}. \end{aligned} \tag{13}$$

For this pure bending problem, the exact transverse shear strains are

$$e_{rt} = e_{st} = 0 \quad \text{in elements-I and II}, \tag{14}$$

and the theoretical relationship among the deflection $w_2 (= w_{tip})$, rotation $\alpha_2 (= \alpha_{tip})$ and rotation $\beta_2 (= \beta_{tip})$ is given, like for beams in the x- and y-directions [3], as

$$w_2 = \frac{1}{2}\alpha_2 = -\frac{1}{2}\beta_2. \tag{15}$$

No anticlastic curvature exists because Poisson's ratio $v = 0$. If a triangular shell element does not show shear locking, Eqs. (14) and (15) should be satisfied.

For element-I, we derive the transverse shear strain field in Appendix, see Eq. (A.3). Using the conditions given in Eqs. (12) and (13) with the symmetry condition $\alpha_2 = -\beta_2$, the transverse shear strain fields for the two elements are for element-I

$$\begin{aligned} e_{rt}^{I} &= \frac{a}{4}\left(w_2 - \frac{1}{2}\alpha_2 - \frac{1}{2}\alpha_4\right) + \frac{1}{3}\hat{c}^{I}(3s-1),\\ e_{st}^{I} &= \frac{a}{4}\left(-\frac{1}{2}\beta_4\right) + \frac{1}{3}\hat{c}^{I}(1-3r) \quad \text{with } \hat{c}^{I} = -\frac{3}{4}ad\alpha_2 \end{aligned} \tag{16}$$

and for element-II

$$\begin{aligned} e_{rt}^{II} &= \frac{a}{4}\left(w_2 + \frac{1}{2}\beta_2 + \frac{1}{2}\beta_4\right) + \frac{1}{3}\hat{c}^{II}(3s-1),\\ e_{st}^{II} &= \frac{a}{4}\left(-\frac{1}{2}\alpha_4\right) + \frac{1}{3}\hat{c}^{II}(1-3r) \quad \text{with } \hat{c}^{II} = \frac{3}{4}ad\beta_2. \end{aligned} \tag{17}$$

With the tying distance $d = 0$, the transverse shear strains vanish with

$$w_2 - \frac{1}{2}\alpha_2 - \frac{1}{2}\alpha_4 = 0, \quad \beta_4 = 0 \quad \text{for element-I}, \tag{18}$$

$$w_2 + \frac{1}{2}\beta_2 + \frac{1}{2}\beta_4 = 0, \quad \alpha_4 = 0 \quad \text{for element-II}. \tag{19}$$

When $\alpha_4 = 0$ in Eq. (18) and $\beta_4 = 0$ in Eq. (19), the pure bending condition is satisfied as follows

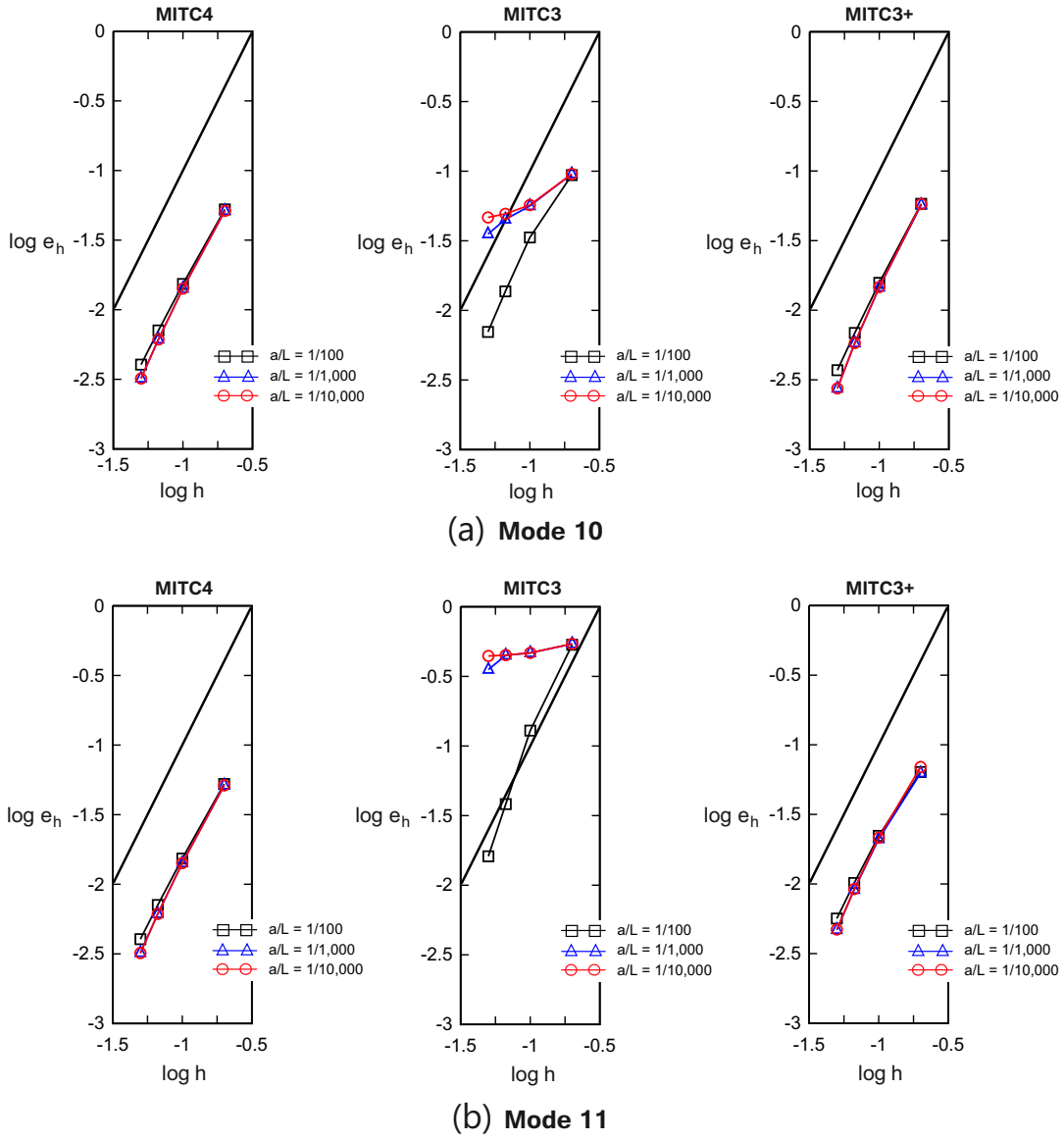

Fig. 15. Convergence curves of the 10th and 11th frequencies for the free square plate problem. The solutions of the shell elements are obtained with uniform $N \times N$ element meshes ($N = 5$, 10, 15 and 20). The bold line represents the optimal convergence rate.

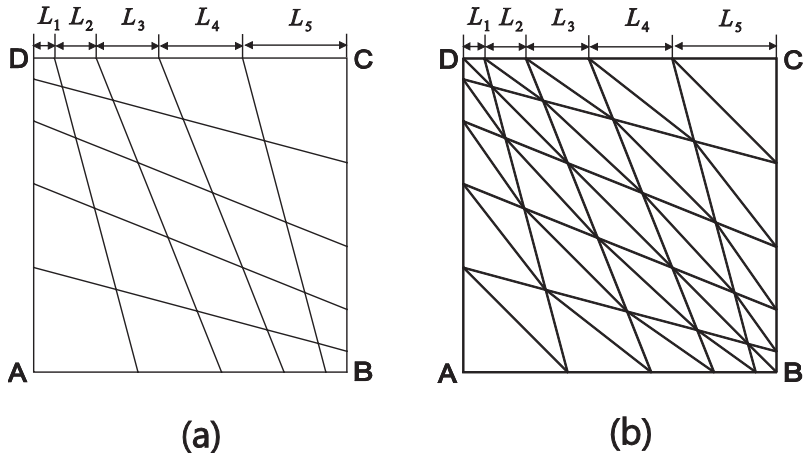

Fig. 16. Distorted mesh pattern for $N = 5$. (a) Mesh pattern used for the MITC4 shell element. (b) Mesh pattern used for the MITC3 and MITC3+ shell elements.

Table 11
Frequencies of the modes 7–11 for the free square plate problem with $N \times N$ distorted meshes shown in Fig. 16 when $a/L = 1/1,000$.

Shell elements	N	Mode number				
		7	8	9	10	11
MITC4	5	21.575	33.071	42.004	57.191	61.420
	10	21.189	31.311	39.109	55.541	56.437
	15	21.087	30.908	38.436	54.892	55.286
	20	21.049	30.757	38.183	54.628	54.851
MITC3	5	22.184	33.780	43.522	62.781	105.68
	10	21.812	32.397	40.587	60.633	93.456
	15	21.692	32.053	39.838	59.615	89.827
	20	21.630	31.829	39.445	58.909	87.021
MITC3+	5	21.817	33.177	43.060	59.889	69.344
	10	21.318	31.546	39.651	56.842	60.559
	15	21.148	31.052	38.734	55.571	57.419
	20	21.079	30.848	38.366	55.026	56.096
Ref.		21.000	30.564	37.864	54.284	54.284

*The reference solutions are obtained by 50×50 element meshes of the MITC4 shell element.

$$w_2 - \frac{1}{2}\alpha_2 = 0, \quad w_2 + \frac{1}{2}\beta_2 = 0. \tag{20}$$

This result shows that the MITC3+ shell element can correctly represent the pure bending conditions in Eqs. (14) and (15) when $d = 0$. Similarly, we tested the MITC3+ shell element in Mesh B and observed that the elements in Mesh B also satisfy the pure bending conditions. Of course, the MITC3 shell element does not satisfy the pure bending conditions in Mesh A and thus shear locking occurs [16].

4.2. Strain energies

Considering three different thicknesses ($a/L = 1/100$, 1/1,000 and 1/10,000), we next solve the two-sided clamped plate problem using the MITC3, MITC3+ and MITC4 shell elements with the applied moments $m_\alpha = m_\beta = 2/L$, see Fig. 11.

Table 8 presents the strain energies calculated using the MITC3, MITC3+ ($d = 0$) and MITC4 shell elements, respectively. Analytically, the calculated strain energy should change in the order of $(a/L)^3$ for this pure bending problem [4]. The MITC3 shell

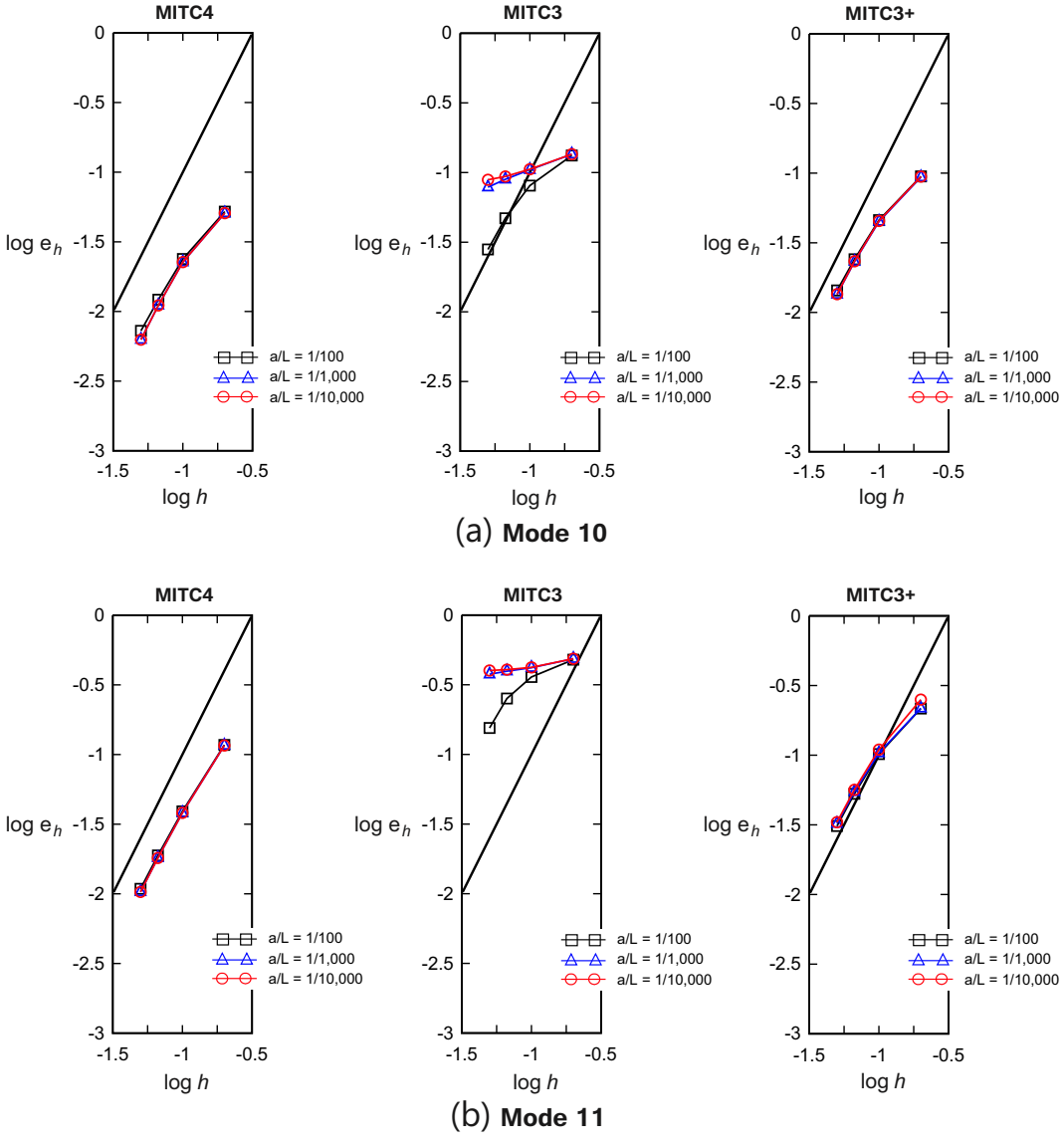

Fig. 17. Convergence curves of the 10th and 11th frequencies for the free plate problem with the distorted meshes shown in Fig. 16. The bold line represents the optimal convergence rate.

element shows correct results only in Mesh B. The MITC3+ shell element shows correct behaviors in both Meshes A and B, although the solutions depend on the mesh patterns. The MITC4 shell element obviously shows excellent results.

Changing the tying distance d in the assumed transverse shear strain field of the MITC3+ shell element, we investigate the strain energy stored in the two-sided clamped plate problem with Mesh A. Four different tying distances are considered: $d = 1/100, 1/1,000, 1/10,000$ and 1/100,000. Table 9 shows that, as the distance d approaches zero, the behavior of the MITC3+ shell element become better.

We note that the bending mode BL1 of the assemblage of two right-angled triangular elements is significantly present in the pure bending displacement field of the problem with Mesh A. Thus, the improved behavior of the MITC3+ shell element is directly due to the alleviation of shear locking in this mode.

5. Dynamic mode solutions

In this section, we perform dynamic mode solutions to investigate the predictive capability of the MITC3 and MITC3+ shell elements in dynamic analysis. Frequencies and modes are calculated and the results are compared with those of the MITC4 shell element. We consider two benchmark problems: a free square plate problem and a free hyperboloid shell problem [1,2,21–27].

For dynamic mode solutions, the following eigenvalue problem is solved

$$\mathbf{K}\vec{\phi}_i^d = \lambda_i^d \mathbf{M}\vec{\phi}_i^d \quad \text{with } i = 1, 2, \ldots, N, \tag{21}$$

where $\mathbf{K}$ and $\mathbf{M}$ is the stiffness and consistent mass matrices, respectively, λ_i^d is the eigenvalue (the square of the free vibration frequency $\omega_i, \lambda_i^d = \omega_i^2$), $\vec{\phi}_i^d$ is the corresponding M-orthonormal

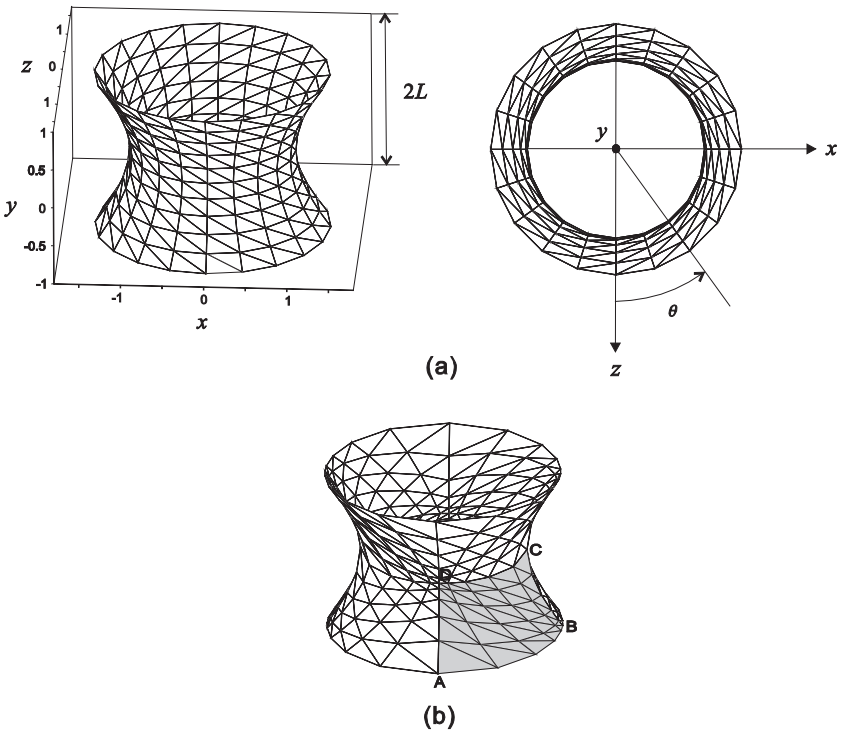

Fig. 18. Free hyperboloid shell problem ($L = 1.0, E = 2.0 \times 10^{11}$, $\nu = 1/3$ and $\rho = 7.8 \times 10^3$). (a) Problem description with a uniform mesh. (b) Distorted mesh pattern.

Table 12
Frequencies of the modes 7–12 for the free hyperboloid shell problem with the $4N \times 2N$ uniform meshes shown in Fig. 18(a) when $a/L = 1/1,000$.

Shell elements	N	Mode number					
		7	8	9	10	11	12
MITC4	5	4.0562	4.0562	6.8339	6.8339	13.163	13.163
	10	4.0089	4.0089	6.7965	6.7965	12.808	12.808
	15	3.9976	3.9976	6.7903	6.7903	12.745	12.745
	20	3.9924	3.9924	6.7882	6.7882	12.721	12.721
MITC3	5	37.449	37.449	149.20	149.20	157.83	157.83
	10	10.029	10.029	35.321	35.321	39.830	39.830
	15	6.0202	6.0202	16.534	16.534	21.429	21.429
	20	4.9650	4.9650	10.734	10.734	16.452	16.452
MITC3+	5	4.1610	4.1610	7.0337	7.0337	13.781	13.781
	10	4.0309	4.0309	6.8420	6.8420	12.969	12.969
	15	4.0091	4.0091	6.8096	6.8096	12.819	12.819
	20	4.0010	4.0010	6.7986	6.7986	12.767	12.767
Ref.		3.9830	3.9830	6.7859	6.7859	12.690	12.690

*The reference solutions are obtained by a 200×100 element mesh of the MITC4 shell element.

eigenvector (dynamic mode), and N is the number of the degrees of freedom [3]. Note that, unlike in a static mode solution, both, the stiffness and mass matrices are considered in dynamics.

To measure the convergence of the finite element solutions, we use the relative error in the reciprocal frequency as follows

$$e_h = \left|\frac{1/\omega_{ref} - 1/\omega_h}{1/\omega_{ref}}\right| = \left|1 - \frac{\omega_{ref}}{\omega_h}\right|, \tag{22}$$

in which ω_{ref} is the reference frequency and ω_h is the calculated frequency of the finite element discretization. The analytical solution is not available for ω_{ref} in the considered benchmark problems. Hence, the reference frequency ω_{ref} is obtained using very fine meshes of the MITC4 shell element.

For the dynamic analysis of the shell problems, the optimal convergence behavior of the frequencies is given by

$$e_h \cong Ch^k, \tag{23}$$

where h denotes the element size. For a 3-node shell element to be uniformly optimal, the value of C must be constant, that is, independent of the shell thickness, and $k = 2$ [3].

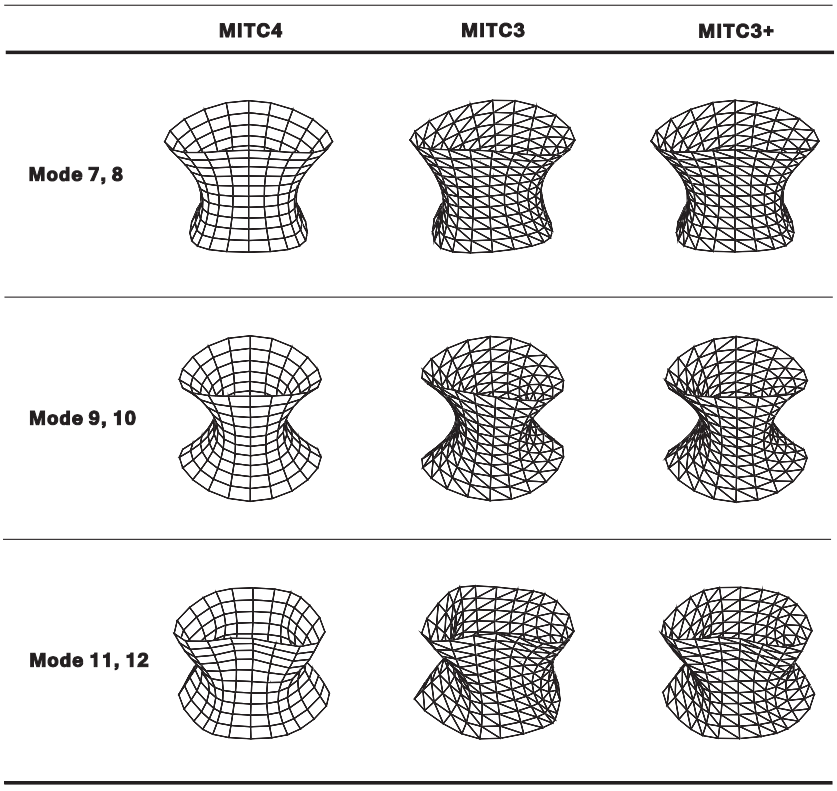

Fig. 19. Shapes of the modes 7–12 for the free hyperboloid shell problem shown in Fig. 18(a) with 20×10 element meshes when $a/L = 1/1,000$.

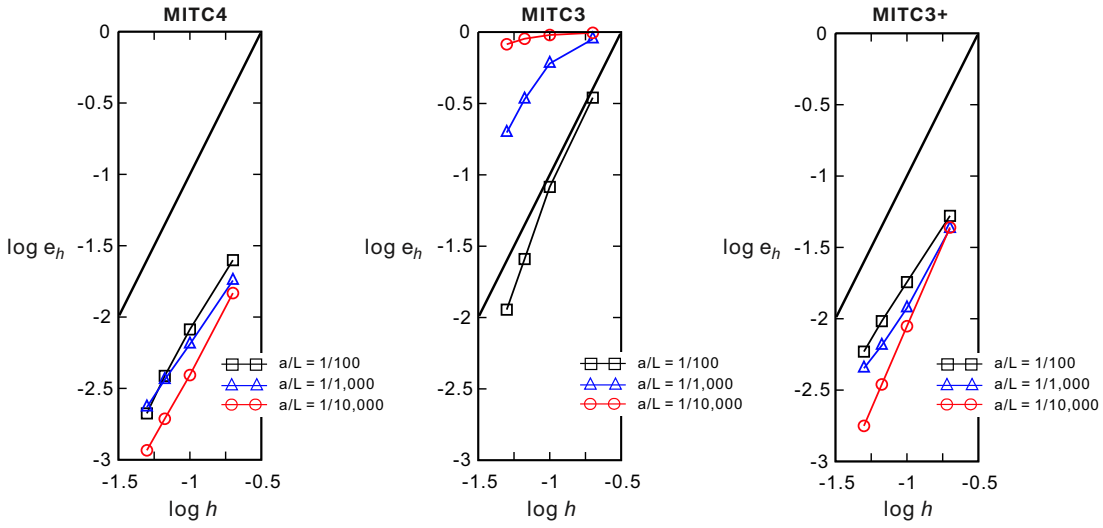

Fig. 20. Convergence curves of the 7th and 8th frequencies for the free hyperboloid shell problem with the uniform meshes shown in Fig. 18(a). The solutions of the shell elements are obtained with uniform $4N \times 2N$ element meshes ($N = 5$, 10, 15 and 20). The bold line represents the optimal convergence rate.

Table 13
Frequencies of the modes 7–12 for the free hyperboloid shell problem with the $4N \times 2N$ distorted meshes shown in Fig. 18(b) when $a/L = 1/1,000$.

Shell elements	N	Mode number					
		7	8	9	10	11	12
MITC4	5	35.751	43.056	44.075	78.905	102.856	123.838
	10	12.537	16.050	17.223	28.059	42.093	43.224
	15	7.8465	9.4797	11.936	16.397	25.840	26.525
	20	6.0587	6.8917	9.7234	11.844	19.647	19.995
MITC3	5	43.052	51.536	168.76	203.23	221.47	228.83
	10	12.338	15.239	44.835	56.487	59.559	80.330
	15	7.2037	8.3684	22.653	29.413	30.099	40.473
	20	5.7356	6.1662	15.218	20.757	21.105	24.968
MITC3+	5	4.6031	4.6142	8.5172	8.5405	15.019	15.034
	10	4.1392	4.1514	7.0032	7.1431	13.316	13.343
	15	4.0347	4.0368	6.8320	6.8816	12.867	12.881
	20	4.0073	4.0090	6.7988	6.8250	12.738	12.748
Ref.		3.9830	3.9830	6.7859	6.7859	12.690	12.690

*The reference solutions are obtained by a 200×100 element mesh of the MITC4 shell element.

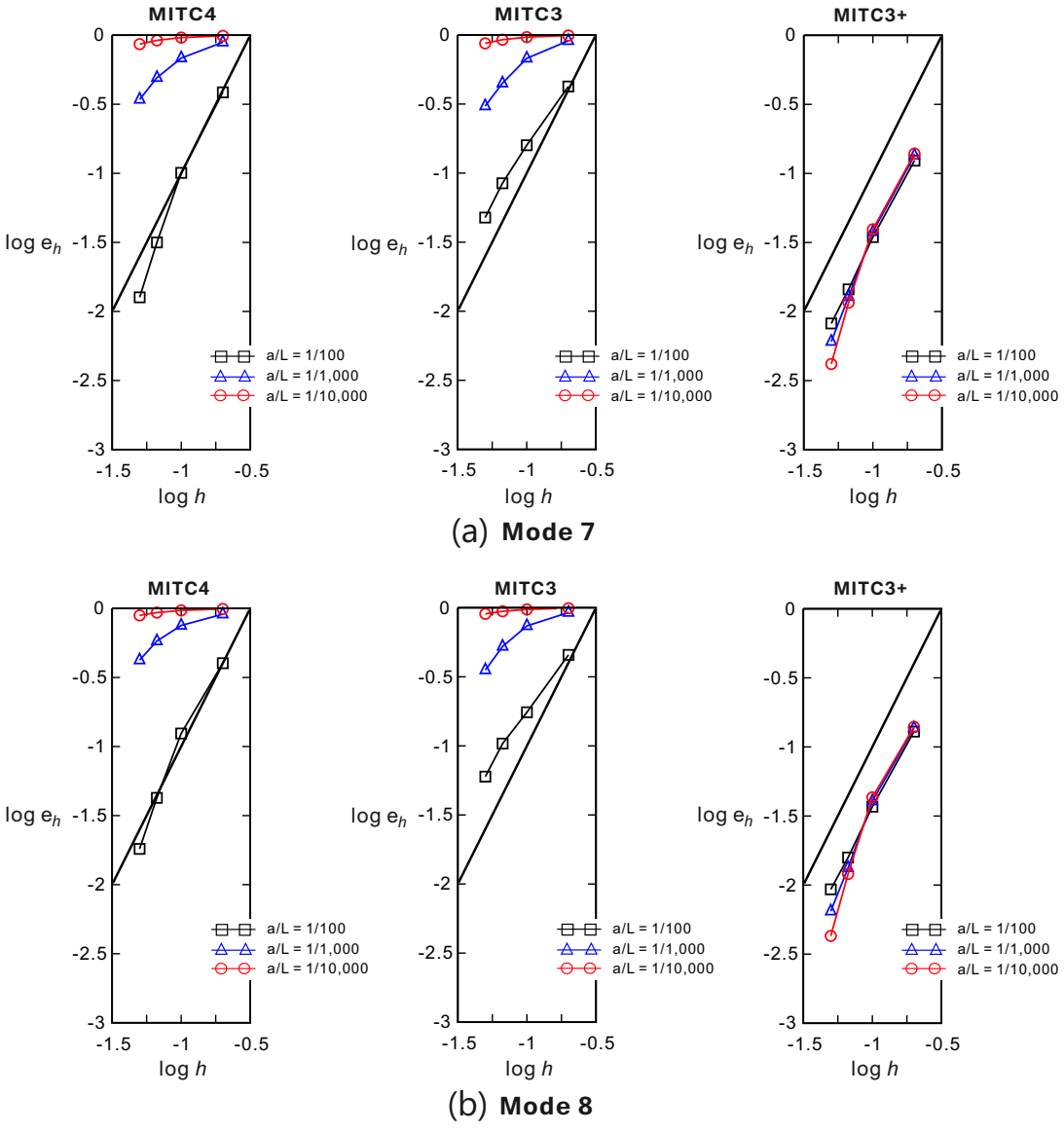

Fig. 21. Convergence curves of the 7th and 8th frequencies for the free hyperboloid shell problem with the distorted meshes shown in Fig. 18(b). The bold line represents the optimal convergence rate.

5.1. Free square plate problem

A free square plate of dimensions $L \times L$ is considered as shown in Fig. 13. We use $L = 1.0, E = 2.07 \times 10^{11}$, $\nu = 0.3$ and density $\rho = 7.8 \times 10^3$. No boundary condition is imposed. We use the reference solutions obtained using a 50×50 element mesh of the MITC4 shell element and verified by Refs. [25,26].

Table 10 presents the frequencies calculated with $N \times N$ element meshes ($N = 5$, 10, 15 and 20) when $a/L = 1/1,000$. The frequencies of the modes 7 to 9 are close to the reference solutions for all tested elements. The frequencies corresponding to modes 10 and 11 should be identical, but this can hardly be the case using triangular shell elements due to the non-symmetry in the mesh patterns used. While the MITC3 shell element produces considerably different frequencies for modes 10 and 11, the MITC3+ shell element shows very similar frequencies for the modes. Using the MITC4 and MITC3+ shell elements produces much more accurate frequencies than obtained with the MITC3 shell element. In Fig. 14, we see that the MITC3 shell element produces a wrong mode shape for the 11th frequency.

The convergence curves of the 10th and 11th frequencies are plotted in Fig. 15. Three different thicknesses ($a/L = 1/100$, $1/1,000$ and $1/10,000$) are considered. The shell finite element solutions are calculated using four different $N \times N$ element meshes ($N = 5$, 10, 15 and 20). We observe that the performance of the MITC3 shell element deteriorates as the thickness decreases, that is, locking occurs. However, the MITC3+ and MITC4 shell elements show, similarly, excellent convergence.

The distorted mesh shown in Fig. 16 is also considered. When an $N \times N$ element mesh is used, each edge is discretized by the following ratio: $L_1 : L_2 : L_3 : \ldots L_N = 1 : 2 : 3 : \ldots N$. Table 11 presents the frequencies with distorted $N \times N$ element meshes ($N = 5$, 10, 15 and 20) when $a/L = 1/1,000$. Fig. 17 shows the convergence curves of the 10th and 11th frequencies. In the both results, the MITC3+ and MITC4 shell elements still show good results even though the predicted modes 10 and 11 are slightly different.

5.2. Free hyperboloid shell problem

We consider the free hyperboloid shell shown in Fig. 18. The mid-surface of the shell structure is given by [1,2]

$$x^2 + z^2 = 1 + y^2; \quad y \in [-1, \quad 1]. \tag{24}$$

We use $L = 1.0, E = 2.0 \times 10^{11}$, $\nu = 1/3$ and density $\rho = 7.8 \times 10^3$. No boundary condition is imposed.

Table 12 presents the frequencies calculated with uniform $4N$ (circumferential direction) $\times$ $2N$ (longitudinal direction) element meshes ($N = 5$, 10, 15 and 20) when $a/L = 1/1,000$. The reference solutions are obtained using a 200×100 uniform mesh of the MITC4 shell elements. For all the elements tested, the frequencies 7, 9 and 11 are identical to the frequencies 8, 10 and 12, respectively. Using the MITC4 and MITC3+ shell elements produces much more accurate frequencies than obtained with the MITC3 shell element. Fig. 19 displays the shapes of the modes 7–12 for uniform 20×10 element meshes, with the shapes of paired modes the same but for a rotation about the y-axis. The mode shapes of the MITC3+ shell element are similar to those of the MITC4 shell element.

Fig. 20 displays the convergence curves of the 7th and 8th frequencies for three different thicknesses: $a/L = 1/100, 1/1,000$, and $1/10,000$. The MITC3+ shell element displays good convergence behaviors similar to the MITC4 shell element. As the thickness decreases, the convergence of the MITC3 shell element becomes worse due to locking.

We also consider the distorted mesh shown in Fig. 18(b). For the shaded region in Fig. 18(b), each edge is discretized as shown in Fig. 16. Table 13 presents the frequencies with distorted $4N \times 2N$ element meshes ($N = 5$, 10, 15 and 20) when $a/L = 1/1,000$. Fig. 21 shows the convergence curves of the 7th and 8th frequencies. In both results, we observe that, while the MITC4 and MITC3 shell elements lock, the MITC3+ shell element still shows good results.

6. Concluding remarks

In this paper, we presented new insight into the static and dynamic modal behaviors of the MITC3+ triangular shell element. For comparison, also the DISP3, MITC3 and MITC4 shell elements were considered.

Detailed static mode solutions were studied for the single right-angled triangular shell elements and the assemblage of two right-angled triangular shell elements. We also investigated the transverse shear strain fields of the MITC3+ shell element in the two-sided clamped plate problem. Through these studies, we found that the MITC3+ shell element formulation contains additional anti-symmetric bending modes (B1+ and B2+) due to the bubble function enrichment, and shear locking is alleviated in these modes using the MITC method. Consequently, unlike the DISP3 and MITC3 shell elements, the MITC3+ shell element performed well in the solution of all cases.

We also performed dynamic mode solutions of an unsupported square plate and a free hyperboloid shell, both representing bending-dominated problems in which locking would be seen, if present. We observed that the MITC3+ shell element shows much better convergence behaviors than the MITC3 shell element. Indeed, the MITC3+ shell element gives as accurate results as the MITC4 shell element in uniform meshes and even significantly better results when distorted meshes are used.

Acknowledgments

This work was supported by the Human Resources Development Program (No. 20134030200300) of the Korea Institute of Energy Technology Evaluation and Planning (KETEP) funded by the Ministry of Trade, Industry and Energy, and the Basic Science Research Program through the National Research Foundation of Korea (NRF) funded by the Ministry of Education, Science and Technology (No. 2014R1A1A1A05007219).

Appendix A. Transverse shear strain fields of the MITC3+ element in flat geometry

The shell finite element can be used for plate bending problems with the following conditions when the geometry is defined on the xy-plane with constant thickness [16]

$$\vec{x}_i = \begin{Bmatrix} x_i \\ y_i \\ 0 \end{Bmatrix}, \quad \vec{u}_i = \begin{Bmatrix} 0 \\ 0 \\ w_i \end{Bmatrix}, \quad \vec{V}_n^i = \vec{i}_z, \quad \vec{V}_1^i = \vec{i}_x, \quad \vec{V}_2^i = \vec{i}_y \quad \text{and} \quad a_i = a \quad \text{for all } i, \tag{A.1}$$

where $\vec{i}_x, \vec{i}_y$ and $\vec{i}_z$ are the unit base vectors in the global Cartesian coordinate system.

From Eqs. (6)–(8), the geometry and displacement interpolations of the MITC3+ shell element are given with the conditions in Eq. (A.1)

$$\vec{x} = \begin{Bmatrix} \sum_{i=1}^{3} h_i x_i \\ \sum_{i=1}^{3} h_i y_i \\ \frac{t}{2} a \end{Bmatrix}, \quad \vec{u} = \begin{Bmatrix} \frac{t}{2} a \sum_{i=1}^{4} f_i \beta_i \\ -\frac{t}{2} a \sum_{i=1}^{4} f_i \alpha_i \\ \sum_{i=1}^{3} h_i w_i \end{Bmatrix}. \tag{A.2}$$

Using Eqs. (9) and (A.2), the transverse shear strain field of the MITC3+ element is given by

$$\begin{aligned}\hat{e}_{rt}^{MITC3+} &= \frac{a}{4}\Big[w_2 - w_1 + \frac{1}{6}(x_2 - 2x_1 + x_3)\beta_1 + \frac{1}{6}(2x_2 - x_1 - x_3)\beta_2 + \frac{1}{2}(x_2 - x_1)\beta_4 \\ &\quad + \frac{1}{6}(2y_1 - y_2 - y_3)\alpha_1 + \frac{1}{6}(y_1 - 2y_2 + y_3)\alpha_2 + \frac{1}{2}(y_1 - y_2)\alpha_4\Big] + \frac{1}{3}\hat{c}(3s - 1), \\ \hat{e}_{st}^{MITC3+} &= \frac{a}{4}\Big[w_3 - w_1 + \frac{1}{6}(x_3 + x_2 - 2x_1)\beta_1 + \frac{1}{6}(2x_3 - x_2 - x_1)\beta_3 + \frac{1}{2}(x_3 - x_1)\beta_4 \\ &\quad + \frac{1}{6}(2y_1 - y_2 - y_3)\alpha_1 + \frac{1}{6}(y_1 + y_2 - 2y_3)\alpha_3 + \frac{1}{2}(y_1 - y_3)\alpha_4\Big] + \frac{1}{3}\hat{c}(1 - 3r) \end{aligned} \quad (A.3)$$

with

$$\hat{c} = \frac{3}{4}ad[(y_2 - y_3)\alpha_1 + (y_3 - y_1)\alpha_2 + (y_1 - y_2)\alpha_3 + (x_3 - x_2)\beta_1 + (x_1 - x_3)\beta_2 + (x_2 - x_1)\beta_3]. \quad (A.4)$$

References

[1] Lee PS, Bathe KJ. Development of MITC isotropic triangular shell finite elements. Comput Struct 2004;82:945–62.
[2] Lee Y, Lee PS, Bathe KJ. The MITC3+ shell element and its performance. Comput Struct 2014;138:12–23.
[3] Bathe KJ. Finite element procedures. Watertown (MA): KJ Bathe; 2014.
[4] Chapelle D, Bathe KJ. The finite element analysis of shells – fundamentals. Second edition. Berlin: Springer-Verlag; 2011.
[5] Chapelle D, Bathe KJ. Fundamental considerations for finite element analysis of shell structures. Comput Struct 1998;66:19–36. 711–712.
[6] Lee PS, Bathe KJ. Insight into finite element shell discretizations by use of the "basic shell mathematical model". Comput Struct 2005;83:69–90.
[7] Lee PS, Bathe KJ. On the asymptotic behavior of shell structures and the evaluation in finite element solutions. Comput Struct 2002;80:235–55.
[8] Beirão da Veiga L. Asymptotic energy behavior of two classical intermediate benchmark shell problems. Math Models Methods Appl Sci 2003;13:1279–302.
[9] Baiocchi C, Lovadina C. A shell classification by interpolation. Math Models Methods Appl Sci 2002;12(10):1359–80.
[10] Bathe KJ, Chapelle D, Lee PS. A shell problem 'highly sensitive' to thickness changes. Int J Numer Methods Eng 2003;57:1039–52.
[11] Dvorkin EN, Bathe KJ. A continuum mechanics based four-node shell element for general nonlinear analysis. Eng Comput 1984;1:77–88.
[12] Bathe KJ, Dvorkin EN. A formulation of general shell elements – the use of mixed interpolation of tensorial components. Int J Numer Methods Eng 1986;22:697–722.
[13] Bucalem ML, Bathe KJ. Higher-order MITC general shell elements. Int J Numer Methods Eng 1993;36:3729–54.
[14] Bathe KJ, Lee PS, Hiller JF. Towards improving the MITC9 shell element. Comput Struct 2003;81:477–89.
[15] Kim DN, Bathe KJ. A triangular six-node shell element. Comput Struct 2009;87:1451–60.
[16] Lee PS, Noh HC, Bathe KJ. Insight into 3-node triangular shell finite elements: the effects of element isotropy and mesh patterns. Comput Struct 2007;85:404–18.
[17] Jeon HM, Lee Y, Lee PS, Bathe KJ. The MITC3+ shell element in geometric nonlinear analysis. Comput Struct 2015;146:91–104.
[18] Argyris JH, Papadrakakis M, Apostolopoulou C, Koutsourelakis S. The TRIC shell element: theoretical and numerical investigation. Comput Methods Appl Mech Eng 2000;182:217–45.
[19] Lee Y, Yoon K, Lee PS. Improving the MITC3 shell finite element by using the Hellinger–Reissner principle. Comput Struct 2012;110–111:93–106.
[20] Kim JH, Kim YH. A three-node C^0 ANS element for geometrically non-linear structural analysis. Comput Methods Appl Mech Eng 2002;191:4035–59.
[21] Jeon HM, Lee PS, Bathe KJ. The MITC3 shell finite element enriched by interpolation covers. Comput Struct 2013;134:128–42.
[22] Lee PS, Bathe KJ. The quadratic MITC plate and MITC shell elements in plate bending. Adv Eng Softw 2010;41:712–28.
[23] Bathe KJ, Lee PS. Measuring the convergence behavior of shell analysis schemes. Comput Struct 2011;89:285–301.
[24] Hiller JF, Bathe KJ. Measuring convergence of mixed finite element discretizations: an application to shell structures. Comput Struct 2003;81:639–54.
[25] Leissa AW. The free vibration of rectangular plates. J Sound Vib 1973;31:257–93.
[26] Mochida Y, Ilanko S. Bounded natural frequencies of completely free rectangular plates. J Sound Vib 2008;311:1–8.
[27] Hernandez E, Hervella-Nieto L, Rodriguez R. Computation of the vibration modes of plates and shells by low-order MITC quadrilateral finite elements. Comput Struct 2003;81:615–28.